Passage of SARS-CoV-2 in cells expressing human and mouse ACE2 selects for mouse-adapted and ACE2-independent viruses

Kexin Yan[1], Troy Dumenil[1], Thuy T. Le[1], Bing Tang[1], Cameron Bishop[1], Andreas Suhrbier[1,2], Daniel J. Rawle[1*].

[1] Immunology Department, QIMR Berghofer Medical Research Institute, Brisbane, Queensland. 4029, Australia.

[2] Australian Infectious Disease Research Centre, GVN Center of Excellence, Brisbane, Queensland, 4029 and 4072, Australia.

[*]Corresponding author. Email: Daniel.Rawle@qimrberghofer.edu.au

SUMMARY

Human ACE2 (hACE2) is required for cell attachment and entry of SARS-CoV-2. Mouse ACE2 (mACE2) does not support infection of early SARS-CoV-2 isolates. Herein we describe a new system for generating mouse-adapted SARS-CoV-2 *in vitro* by serial passaging virus in co-cultures of cell lines expressing hACE2 and mACE2. Mouse-adapted viruses emerged with a series of spike protein amino acid changes, all of which have been reported in human isolates. Mouse-adapted viruses replicated to high titers in C57BL/6J mouse lungs and nasal turbinates, and caused severe lung histopathology. Remarkably, one mouse-adapted virus was able to replicate efficiently in ACE2-negative cell lines, a characteristic not described for any SARS-CoV-2 variants. ACE2-independent entry by SARS-CoV-2 represents a new biology for SARS-CoV-2 with potential widespread implications for disease and intervention development.

INTRODUCTION

Severe acute respiratory syndrome coronavirus 2 (SARS-CoV-2) emerged in 2019, causing a global pandemic of coronavirus disease 2019 (COVID-19) (1). SARS-CoV-2 spike protein binds the human ACE2 (hACE2) receptor for cell attachment and entry (2). ACE2 binding has a deep ancestral origin in the sarbecovirus lineage of coronaviruses (3). SARS-CoV, SARS-CoV-2, and SARS-related bat coronaviruses all use ACE2 as their entry receptor (4). The ACE2 binding capacity of the receptor binding motif (RBM), within the receptor binding domain (RBD), has high plasticity, with genetically diverse spike proteins able to bind ACE2 (3, 4). The SARS-CoV-2 variants of concern (Alpha, Beta, Gamma, Delta and Omicron), all require ACE2 binding for efficient infection (5, 6). However, Puray-Chavez et al identified that SARS-CoV-2 containing the E484D amino acid change replicated in the ACE2-negative H522 cell line (7).

The ancestral isolates of SARS-CoV-2 (Wuhan strain) are unable to use mouse ACE2 (mACE2) to support infection (2), and to study these viruses a series of mouse models were developed that express hACE2 (2, 8-10). Some subsequent variants of SARS-CoV-2 emerged to be able to use mACE2, including Alpha, Beta and Gamma, but not Delta (6). In addition, mouse-adapted SARS-CoV-2 have been produced by serial passage of the ancestral SARS-CoV-2 in mouse lungs (11-15) or by reverse genetics (16) to introduce amino acid changes that allow binding to mACE2.

As infection of wild animals by SARS-CoV-2 is increasingly being reported (17-21), we sought to investigate further the process of mouse adaptation. We have previously reported the use of HEK293T cells that express hACE2 (HEK293T-hACE2) and mACE2 (HEK293T-mACE2) by virtue of lentiviral transduction, with the former but not the latter able to support efficient replication of ancestral SARS-CoV-2, hCoV-19/Australia/QLD02/2020 (SARS-CoV-

66 2_{QLD02}) (2). Herein we used serial passage of SARS-CoV-2_{QLD02} in co-cultures of HEK293T-
67 hACE2 and HEK293T-mACE2 to generate five distinct mouse-adapted viruses that were able to
68 replicate in both HEK293T-hACE2 and HEK293T-mACE2 cells. These viruses also replicated
69 in C57BL/6J mouse lungs and nasal turbinates, leading to characteristic COVID-19
70 histopathological lesions. Remarkably, one of these viruses was also able to replicate in
71 HEK293T cells in the absence of ACE2 transduction. This virus was also able to replicate in a
72 number of other cell lines that ordinarily do not support SARS-CoV-2 infection unless
73 genetically altered to express ACE2. This represents the second report of ACE2-independent
74 infection by SARS-CoV-2 (7), with potential implications for the biology of SARS-CoV-2
75 infections, SARS-CoV-2 evolution, and intervention development.

76

77 **RESULTS**

78 **SARS-CoV-2 passaging in co-cultures of hACE2 and mACE2-expressing cells selects for**
79 **mACE2-adapted virus**

80 To investigate further the process of mouse adaptation, we undertook SARS-CoV-2
81 adaptation to mACE2 by passaging in co-cultures of HEK293T cells expressing mACE2 (herein
82 called HEK293T-mACE2) and cells expressing hACE2 (HEK293T-hACE2) (Fig. 1A). An
83 alternative to HEK293T-hACE2 cells was also used: HEK293T cells expressing mACE2
84 containing the N31K and H353K mouse-to-human amino acid changes (HEK293T-mACE2-
85 N31K/H353K), which supports SARS-CoV-2 replication as we described previously (2). SARS-
86 CoV-2 was passaged in three parallel co-cultures of HEK293T-mACE2 + HEK293T-hACE2 and
87 three parallel co-cultures of HEK293T-mACE2 + HEK293T-mACE2-N31K/H353K.

To determine whether passaged SARS-CoV-2 can utilize mACE2 for replication, HEK293T-mACE2 cells were infected and virus titer was determined by $CCID_{50}$ assays at 0 and 72 hours post infection. This was first tested using passage 4 supernatant, and no virus replication was detected (Fig. 1B). Cytopathic effect (CPE) was first observed in co-cultured HEK293T-mACE2 cells at passage 9 (Fig. 1A), and virus from 5 out of 6 parallel co-cultures replicated in HEK293T-mACE2 cells, although one replicated poorly (Fig. 1C). Significant CPE in HEK293T-mACE2 cells was evident for the replicate with the highest virus titer (herein called MA1), while all others had minor CPE (Fig. 1D). This confirmed that SARS-CoV-2 after nine passages in hACE2 and mACE2 co-cultures evolved to replicate in mACE2-expressing cells.

To determine if these mACE2-adapted viruses are able to infect wild-type mice, C57BL/6J mice were infected by intrapulmonary inoculation with 1.5×10^4 $CCID_{50}$ per mouse. At 2 days post infection mice were euthanized and virus titer in lungs measured by $CCID_{50}$ assay. All five MA viruses replicated in mouse lungs (Fig. 1E). Three of these replicated to above 10^6 $CCID_{50}$/g, while the other two were below 10^5 $CCID_{50}$/g (Fig. 1E). The viruses were numbered MA1 to MA5 in order of lung titer, with MA1 and MA3 derived from HEK293T-mACE2 + HEK293T-hACE2 co-cultures, and MA2, MA4 and MA5 from HEK293T-mACE2 + HEK293T-mACE2-N31K/H353K co-cultures. This indicates that *in vitro* adaptation to mACE2 also permitted SARS-CoV-2 replication in wild-type mice.

All spike amino acid changes in mACE2-adapted SARS-CoV-2 have been reported in human isolates

To determine the mutations in the SARS-CoV-2 genome after co-culture passaging, viral RNA from cell culture supernatant (Fig. 1C) and mouse lungs (Fig. 1E) were sequenced by standard RNA-Seq. There were 15 unique non-synonymous amino acid changes and two

deletions in spike across the five different MA viruses (Fig. 2A). The non-spike amino acid changes include nine unique amino acid changes in Orf1ab and an 11 amino acid deletion in Orf3a (Fig. 2A). Virus from cell culture supernatant had almost identical sequences to virus after one passage in mouse lungs (Supplementary Table 1), indicating no further *in vivo* adaptation.

Of the 15 changes in spike, nine were outside the receptor binding domain (RBD) (Fig. 2B). All five viruses contained the D215G change (Fig. 2A), and this was already 11% of the QLD02 virus stock population (Supplementary Table 1). The deletion of the QTQTN flanking sequence of the furin cleavage site was also present in all five viruses, and commonly arises after *in vitro* passage of SARS-CoV-2 (22). MA1 contained the P812L change in the S2' cleavage site. N74T was present in MA2, which removes a glycosylation site (23). MA3 contained deletion of amino acids 69-72, accompanied with the I68R amino acid change (Fig. 2). This is similar to the 69-70 deletion, which compensates for amino acid changes that impair infectivity in the Alpha variant (24). W64R, present in MA4, consistently arose after *in vitro* passage of spike-pseudotyped vesicular stomatitis virus (VSV) in hACE2-expressing cells (25). The other amino acid changes (E98A in MA1 and D796N in MA3) have unknown implications. Across the five MA viruses there were five different residues that were changed in the spike RBD; R408G, E484D, Q493R/K, Q498H and N501T (Fig. 2B).

All amino acid changes in the MA viruses were identified in human SARS-CoV-2 isolates (Fig. 2C and Supplementary Figure 1). Prevalence for the deletion of amino acids 69-70 was 22% and is a hallmark of the Alpha and Omicron variants (Fig. 2B). D215G was in 7.7% of human isolates and is a hallmark of the Beta variant. The next most prevalent spike amino acid change was P812L, which forms 0.1% of isolates, but is not a hallmark of any variants of

concern. The N501T amino acid change is in 0.09% of isolates, while N501Y is present in Alpha, Beta, Gamma and Omicron variants. Q493R was identified in just 0.0053% of isolates, although this amino acid change is in the newly emerged Omicron variant, and thus this percentage is expected to increase. Omicron variant contains the Q498R amino acid change, which introduces a positive charge at this residue similarly to the Q498H change in MA1 (Supplementary Figure 2). Beta, Gamma and Omicron variants have E484 amino acid changes, although these are less conservative than E484D in MA1. E484A in Omicron may have a similar effect to E484D, with both changes reducing the stretch of the E484 negative charge, and potentially exposing adjacent residues to new interactions (Supplementary Figure 2). However, it is difficult to predict how the Omicron variant E484A and Q498R amino acid changes behave in the context of the other 13 changes in the RBD (Supplementary Figure 2).

Modelling the spike RBD changes indicate the Q493R/K and Q498H increase interactions with mACE2

The amino acid changes in the RBD (R408G, E484D, Q493R/K, Q498H and N501T) were modelled to determine their effect on mACE2 binding. R408G in MA2 removed a bulky side chain protruding from the RBD (Supplementary Figure 3), which may make the ACE2-interface of the RBD more accessible to receptor binding. E484D in MA1 has been described as allowing for ACE2-independent entry (26), and amino acid changes at this site are thought to be involved in antibody escape (27). E484D is a conservative change that does not significantly affect predicted interactions with ACE2, but reduces the reach of the negative charge at this residue (Fig. 3), potentially exposing proximal residues to new interactions. Q493K or Q493R was selected for in 4/5 viruses, and is a key change in mouse adapted SARS-CoV-2 (11, 13). Modelling predicted that Q493K/R had substantially increased interactions with mACE2 via N31

(Fig. 3). Q498H is a key change in mouse adapted SARS-CoV-2 (12, 13), and modelling predicted that this change had substantially increased interaction with mACE2 via Y41 and H353 (Fig. 3). N501T was selected in all three HEK293T-mACE2 + HEK293T-mACE2-N31K/H353K co-cultures, but none of the HEK293T-mACE2 + HEK293T-hACE2 co-cultures. N501T is selected in mink (20) and ferrets (28). N501T is a conservative change and modelling indicated that N501T did not significantly affect interactions with mACE2 H353 (Fig. 3).

This study continued investigations using MA1 and MA2 since these viruses had the highest virus titers in mouse lungs (Fig. 1E), and contained distinct spike amino acid changes from one another (Fig. 2A) while MA3, MA4 and MA5 contained amino acid changes similar to MA2. Mouse lung homogenate for MA1 and MA2 was used to inoculate HEK293T-mACE2 cells and virus harvested on day 2 post-infection was aliquoted and stored as virus stocks (Fig. 1A).

MA1 replicates in ACE2-negative cell lines

Growth kinetics of MA1 and MA2 were compared with SARS-CoV-2_{QLD02}, as well as the Alpha and Beta variants, in HEK293T cells expressing hACE2, mACE2, or neither. All viruses replicated in HEK293T-hACE2 cells (Fig. 4A), and all viruses except SARS-CoV-2_{QLD02} replicated in HEK293T-mACE2 cells (Fig. 4B). This highlights the ability of newly emerged SARS-CoV-2 variants to replicate in mice (6). Unsurprisingly, MA1 and MA2 replicated significantly faster in HEK293T-hACE2 and HEK293T-mACE2 cells compared to SARS-CoV-2_{QLD02}, Alpha and Beta variants (Fig. 4A-B), indicating adaptation to these cell lines. Remarkably, MA1 replicated to high titers in HEK293T cells not transduced with ACE2 (Fig. 4C), indicating evolution of an ACE2-independent entry mechanism. MA2 also replicated in untransduced HEK293T cells, however this was significantly lower than for MA1 (Fig. 4C).

ACE2-independent replication was not observed for SARS-CoV-2_{QLD02}, Alpha or Beta variants (Fig. 4C). We have thus generated two mACE2-adapted SARS-CoV-2 viruses, including one with a robust ACE2-independent entry mechanism.

Since MA1 had robust replication in ACE2-negative HEK293T cells, we sought to determine if MA1 also replicated in other cell lines that ancestral SARS-CoV-2 does not normally infect. 3T3 (mouse embryonic fibroblast), AE17 (mouse lung mesothelioma cells), A549 (adenocarcinomic human alveolar basal epithelial cells), HeLa (cervical cancer cells) and LLC-PK1 (pig kidney epithelial cells) are not normally infected by ancestral SARS-CoV-2 isolates (2, 29, 30), confirmed herein (Fig. 4D-H). We also confirmed using publically available RNA-Seq data that HEK293T, 3T3, HeLa and A549 cells express negligible ACE2 mRNA (Supplementary Figure 4). MA1 was able to replicate in all of the aforementioned cell lines (Fig. 4D-H), with the highest titers observed in 3T3 cells (Fig. 4D) and LLC-PK1 cells (Fig. 4H). Beta variant (hACE2 or mACE2-dependent) did not replicate in mouse 3T3 or AE17 cells (Fig. 4D-E), indicating mACE2 was not available as an entry receptor in these cells. MA2 replicated poorly in 3T3 cells (Fig. 4D), and did not replicate in AE17 cells (Fig. 4E). A previous study showed that pig ACE2 is able to support SARS-CoV-2 entry (31), thus the lack of QLD02 replication in LLC-PK1 cells suggests that pig ACE2 was not accessible as an entry receptor. Antibody staining of ACE2 has been detected in the cytoplasm, but not the cell surface, of LLC-PK1 cells (32). Overall, the data suggests that the ACE2-independent entry mechanism of MA1 is robust and conserved across several different cell lines from several different species.

ACE2-independent infection of HEK293T cells by MA1 is optimal when cells are adherent

To determine if the ACE2-independent entry receptor is susceptible to trypsin cleavage, we infected HEK293T or HEK293T-hACE2 cells with MA1 after detachment using trypsin, a

trypsin-like enzyme (TrypLE), citric saline, or by mechanical detachment. Cells were infected in 96 well plates at low MOI (0.01), incubated for 4 days and crystal violet staining used to measure cell survival and CPE. The detachment method did not affect infection efficiency (Supplementary Figure 5), arguing against trypsin cleavage of the alternate receptor being a major inhibitor of infection. However, MA1 infection of HEK293T cells was less efficient when infected in suspension (regardless of detachment method) compared to when infected after seeding overnight. HEK293T-hACE2 cells were infected efficiently while in suspension (Supplementary Figure 5), indicating hACE2 expression was not altered by detachment. This suggests that the ACE2-independent entry factor for MA1 was less available for virus binding when cells were detached from the tissue culture dish and infected in predominantly single cell suspensions.

mACE2-adapted SARS-CoV-2 replicates to high titers in C57BL/6J mouse lung bronchial epithelium and nasal turbinates

To determine utility of MA1 and MA2 as a mouse model of SARS-CoV-2 infection and COVID-19, C57BL/6J mice were infected by intrapulmonary inoculation with 10^5 $CCID_{50}$ MA1 or MA2 per mouse. Mouse lungs and nasal turbinates were harvested at day 2, 4 and 7 post-infection, and heart, brain, small intestine, colon, liver, kidney and spleen were harvested on day 2 and 4 post infection. Virus titer peaked in lungs on day 2 reaching 6-8 $\log_{10}$ $CCID_{50}$/g, before dropping to 3-5 $\log_{10}$ $CCID_{50}$/g on day 4 (Fig. 5A). By day 7, half of the mice had undetectable virus titer, while the other half had virus titer just above the limit of detection (Fig. 5A). There was no significant difference between MA1 or MA2 virus titers in the lungs at any time points.

Nasal turbinate titers also peaked on day 2, with titers significantly higher for MA1 (7-8 $\log_{10}$ $CCID_{50}$/g) compared to MA2 (6-7 $\log_{10}$ $CCID_{50}$/g) (Fig. 5B). On day 4 nasal turbinate

titers had dropped to 3-5 $\log_{10}$ $CCID_{50}$/g, and was mostly undetectable on day 7 (Fig. 5B). Apart from two mice with low MA1 virus titers detected in the heart on day 2, virus titers were not detected in brain, small intestine, colon, liver, kidney or spleen for any mice (Fig. 5C). There was no significant weight loss observed for MA1 or MA2 infected mice (Fig. 5D).

Immunohistochemistry (IHC) staining with anti-SARS-CoV-2 spike monoclonal antibody showed that virus replication was localized primarily to bronchial epithelium in MA1 and MA2 infected C57BL/6J mice lungs (Fig. 5E). Focal regions of virus replication in bronchial epithelium were abundant at day 2, rare at day 4, and not detected at day 7 (Fig. 5E), which matched the pattern of lung virus titer (Fig. 5A). Bronchial epithelial staining is consistent with other mouse-adapted SARS-CoV-2 viruses (13, 16, 33), and infection of mACE2 promoter-driven hACE2 mice infected with non-mouse adapted viruses (Fig. 5E) (34). This is in contrast to alveolar epithelial cell tropism of SARS-CoV-2 in K18-hACE2 mice (Fig. 5E) (34).

mACE2-adapted SARS-CoV-2 induces severe lung histopathology in wild-type mice

Mouse lungs at day 2, 4 and 6 were fixed in 10% formalin, and hematoxylin and eosin (H&E) stained lung sections were examined for histopathological lesions. MA1 and MA2 SARS-CoV-2 infected mice lungs had severe histopathological lesions including bronchiolar sloughing, smooth muscle hyperplasia, collapse of alveolar spaces, and bronchial bleeding and oedema (Fig. 6A). There was no discernible difference in lesion severity between timepoints or virus strain. The ratio of blue to red pixels in H&E stained sections is a measure of cellular infiltration (35). Lungs from mice infected with either MA1 or MA2 had significantly higher cellular infiltration compared to uninfected mice (Fig. 6B). There was no significant difference between MA1 compared to MA2, or between timepoints (Fig. 6B). Automated quantitation of white space in lung sections is a measure of lung consolidation (10), and MA1 SARS-CoV-2

infected mice had significantly more lung consolidation (less white space) on day 7 (Fig. 6C). MA1 infected mice on day 4 and MA2 infected mice on day 7 had reduced white space on average, however this did not reach significance (Fig. 6C). Overall these analyses indicate severe lung histopathology after mice lung infection with MA1 or MA2, with lesions similar to that of infected K18-hACE2 mice lungs (10).

DISCUSSION

Herein we describe a new technique to generate mouse-adapted SARS-CoV-2, with applicability in studying virus evolutionary pressures *in vitro*. We show that SARS-CoV-2 infection of HEK293T co-cultures expressing hACE2 and mACE2 leads to selection of viruses that can replicate in mACE2 expressing cells. Each of these viruses contained a distinct constellation of mutations in the Spike protein, highlighting multiple ways of adaptation to mACE2. These viruses also replicated to high titers in mouse lungs and nasal turbinates, and caused severe lung histopathology. The mouse adapted viruses developed herein adds to the repertoire of other mouse adapted SARS-CoV-2 that can be used for mouse models of COVID-19 (11-14, 16). Incidentally, an ACE2-independent SARS-CoV-2 virus also emerged, and is the second report of ACE2-independent infection by SARS-CoV-2 (7).

ACE2 is lowly expressed in lung and trachea (36), thus evolution of alternative receptor usage may affect virus tropism, pathology and disease. Remarkably, one of the viruses that emerged from co-culture passaging did not require ACE2 for cell entry, and replicated efficiently in ACE2-negative cell lines. Puray-Chavez *et al.* found that SARS-CoV-2 containing the E484D change replicated in an ACE2-negative cell line (H522 human lung adenocarcinoma cells), however while they speculate on a role for heparin they did not identify the alternate receptor

(37). MA1 contains the same E484D change, providing further evidence that E484D allows replication in the absence of ACE2. E484D is a very conservative change and slightly reduces the reach of the negative charge at this residue, which may allow the alternate receptor better access to surrounding residues, such as Y489 and F490 (Supplementary Figure 2). A number of alternate receptors have been suggested for SARS-CoV-2, including DC-SIGN/L-SIGN (38), Kidney Injury Molecule-1/T cell immunoglobulin mucin domain 1 (KIM-1/TIM-1) (32), AXL Receptor Tyrosine Kinase (36), neuropilin 1 (NRP1) and CD147 (39). These alternate receptors are not expressed in HEK293T cells and only facilitated entry of ancestral SARS-CoV-2 when introduced into HEK293T or other cell lines, and thus likely do not explain the robust replication of MA1.

Many have speculated that integrins, which are highly expressed in lungs, could be a potential SARS-CoV-2 entry receptor (40-45). Integrins mediate cell line adhesion to cell culture vessels, and thus may be downregulated or altered after detachment, with detachment reducing MA1 infection. SARS-CoV-2 contains an 'RGD' motif in the spike RBD (Supplementary Figure 6), and this motif commonly binds cell surface integrins (43). The ACE2-negative cell lines that supported MA1 replication express a range of integrins (Supplementary Figure 7). It is possible that the E484D and/or Q498H amino acid changes in MA1 (and A484 and R498 in Omicron) increase accessibility of the RGD motif for integrin binding, however this is difficult to determine using PyMOL modelling (Supplementary Figure 6). Cele *et al*. has indicated that the Omicron variant requires ACE2 for infection of H1299 cells (human non-small cell lung carcinoma) (5). Whether the Omicron variant, which contains some amino acid changes similar to MA1, has evolved ACE2-independence should be further investigated in other ACE2-negative cell lines such as HEK293T, A549, 3T3 and HeLa.

A previous study showed that the RBD changes in the MA viruses did not greatly impact hACE2 binding affinity compared to parental SARS-CoV-2; Q498H = K_D $\Delta\log_{10}$ +0.3, N501T = K_D $\Delta\log_{10}$ +0.1, E484D = K_D $\Delta\log_{10}$ -0.38, Q493R/K K_D $\Delta\log_{10}$ -0.09 and R408G K_D $\Delta\log_{10}$ -0.08 (for comparison, L461D = K_D $\Delta\log_{10}$ -4.8) (46). This argues against the possibility that MA1 had greatly increased ACE2 affinity that allows replication in cells that express low levels of ACE2, and further suggests an ACE2-independent mechanism.

A potential limitation of these mouse adapted SARS-CoV-2 viruses is deletion of the QTQTN furin cleavage site flanking sequence, which impairs S1/S2 cleavage by furin (47). Prior S1/S2 cleavage is required for S2' cleavage by transmembrane protease serine 2 (TMPRSS2) at the cell surface, which is important for entry in TMPRSS2 positive cells. The QTQTN deletion commonly arises after virus propagation in TMPRSS2 negative cell lines (such as Vero E6 and HEK293T), although this deletion is also evident in some human clinical samples (47). This deletion improves cleavage by Cathepsin L, which substitutes for TMPRSS2 by cleaving S2' in endosomes and releasing viral RNA into the cytoplasm (48). Other studies have shown that deletion of the furin cleavage site attenuates replication in hamsters and K18-hACE mice (49) and reduces transmission in ferrets (50). Our data suggests that this deletion didn't dramatically affect mouse adapted virus replication or tropism in C57BL/6J mouse lungs compared to other studies (11), although side-by-side comparison with virus containing the same spike amino acid changes as MA1 and MA2 but maintaining furin cleavage would be needed to determine if there is any attenuation. The D614G change, which is present in all SARS-CoV-2 variants (except the ancestral Wuhan strain), also increases virus stability and entry via the cathepsin L route (48). Cathepsin L is widely expressed in human nasal and lung epithelial cells (48), thus our mouse adapted viruses, which likely rely on cathepsin L cleavage rather than

furin/TMPRSS2, still models legitimate human and mouse infections and may be more useful for investigating cathepsin L inhibitors (51, 52).

Lung titers for MA1 and MA2 infected mice were broadly comparable to other mouse adapted SARS-CoV-2 studies that had lung titers at ~10^6 plaque forming units (pfu) per tissue on day 2, and declining titers thereafter (11, 16). However, these studies reported nasal turbinate/cavity titers significantly lower than lung titers, while our MA1 and MA2 viruses infected nasal turbinates at similar levels to lungs. Whether MA1 and MA2 have different properties to other mouse adapted viruses that allow more robust nasal turbinate infections, or whether there are sampling differences between studies, is not known. Some studies have reported ~10% weight loss in C57BL/6J mice after infection with mouse adapted SARS-CoV-2 that had been passaged *in vivo* 15 times (11, 53), suggesting this technique may yield viruses with higher mouse pathogenicity than *in vitro* mACE2-adaptation, which did not cause significant weight loss. There was no significant virus replication in any non-pulmonary organs, which is consistent with other mouse adapted SARS-CoV-2 models (13), and likely better reflects human organ tropism compared to the widely used K18-hACE2 transgenic mouse model which succumbs to fulminant brain infection (54).

In summary, we introduce a novel *in vitro* technique for selection of desired viral attributes, in this case SARS-CoV-2 mACE2 binding. Passaging of SARS-CoV-2 in co-cultures of cells expressing hACE2 and mACE2 provided mouse adapted virus, but also ACE2-independent virus. While others have identified alternative receptors of ancestral SARS-CoV-2, few have identified mutant SARS-CoV-2 that replicates in the absence of ACE2 and the absence of the currently identified alternate receptors. We have thus identified a potentially critical new outcome of SARS-CoV-2 evolution, the development of ACE2-independence, which may have

widespread implications for disease and intervention development

ACKNOWLEDGEMENTS

From QIMR Berghofer Medical Research Institute we thank Dr I Anraku for managing the PC3 (BSL3) facility and animal house staff for mouse breeding and agistment. We thank Dr Alyssa Pyke and Mr Fredrick Moore (Queensland Health, Brisbane) for providing the SARS-CoV-2 isolates. We thank Dr Clay Winterford for the histology and immunohistochemistry. We thank Paul Collins for library preparation and RNA-Seq. We thank Monash Genome Modification Platform for providing the plasmid containing the mouse-codon optimized human ACE2 gene. We thank Clive Berghofer and the Brazil Family Foundation (and many others) for their generous philanthropic donations to support SARS-CoV-2 research at QIMR Berghofer. The project was also partly funded by an intramural seed grant from the Australian Infectious Diseases Research Centre. A.S. holds an Investigator grant from the National Health and Medical Research Council (NHMRC) of Australia (APP1173880).

AUTHOR CONTRIBUTIONS

Conceptualization, D.J.R.; Methodology, D.J.R. and A.S.; Formal analysis, D.J.R., A.S., T.D., C.B.; Investigation, D.J.R., K.Y., T.T.L., and B.T.; Resources, A.S.; Data curation, D.J.R., A.S., and T.D.; Writing – original draft, D.J.R.; Writing – review and editing, A.S. and D.J.R.; Visualization, D.J.R., A.S., and T.D.; Supervision, D.J.R. and A.S., Project administration, D.J.R. and A.S.; Funding acquisition, A.S. and D.J.R.

DECLARATION OF INTERESTS

The authors declare no competing interests.

DATA AVAILABILITY

All raw sequencing data (fastq files) will be made available from the Sequence Read Archive (SRA), BioProject accession: To be uploaded in due course. All other data is available within the paper and supporting information files.

FIGURE LEGENDS

Figure 1. SARS-CoV-2 *in vitro* adaptation for mACE2 utilization. A) Schematic of SARS-CoV-2 passaging in hACE2/mACE2 co-cultures. Co-cultures were infected with SARS-CoV-2 and passaged 9 times, and then passaged 3 times in HEK293T-mACE2 cells. C57BL/6J mice were infected by intrapulmonary inoculation, and lungs harvested at day 2 post-infection for titration or to produce virus stocks by infecting HEK293T-mACE2 cells. Supernatant at passage 4 **(B)** or passage 9 **(C)** was used to infect HEK293T-mACE2 cells and supernatant was titered at 0 or 72 hours post-infection by $CCID_{50}$ assay. **D)** Inverted light microscopy images of HEK293T-mACE2 cells infected with passage 9 supernatants at 72 hours post-infection. Images are representative of at least three replicates. **E)** Lung tissue titer per gram by $CCID_{50}$ assay at day 2 post-infection for C57BL/6J mice infected with SARS-CoV-2_{QLD02} (n=6) or MA1-5 (n=5).

Figure 2. Sequence analyses of mACE2 adapted SARS-CoV-2. A) Amino acid changes in SARS-CoV-2 MA1, MA2, MA3, MA4 and MA5 as determined by RNA-Seq (full dataset in Supplementary Table 1). Amino acid changes that only appear in one MA virus are in red, with other colors used to show amino acid changes common between at least two MA viruses. **B)** Spike amino acids with changes in any of the MA viruses are shown in red on the structure of

spike bound with human ACE2 (PDB: 7DF4). **C)** Spike amino acid changes and their prevalence in human isolates (using CoV-GLUE-Viz), and presence in variants of concern (Alpha, Beta, Gamma, Delta, Omicron). Color coding refers to similarity of the MA amino acid compared to the variant of concern amino acid; green = exact match, blue = conservative, orange = non-conservative.

Figure 3. Modelling RBD amino acid changes for interactions with mACE2. The mutagenesis function in PyMOL was used to mutate the structure of SARS-CoV-2 spike bound human ACE2 (PDB: 7DF4). Green = ACE2. Yellow = hACE2 residues changed to mACE2. Blue = SARS-CoV-2 spike RBD. Red = RBD residues changed in any MA virus. Magenta = RBD residues changed in the indicated MA virus. Light blue shading = areas of interaction between indicated RBD residues and ACE2. Black dotted interactions represent hydrogen bonds, and yellow dotted lines represent any interactions within 3.5 Å.

Figure 4. *In vitro* growth kinetics of mACE2-adapted viruses reveal ACE2-independent entry mechanism. **A)** HEK293T-hACE2, **B)** HEK293T-mACE2, **C)** untransduced HEK293T, **D)** 3T3, **E)** AE17, **F)** A549, **G)** HeLa or **H)** LLC-PK1 were infected with the indicated SARS-CoV-2 viruses (red = QLD02, green = Alpha, magenta = Beta, black = MA1, blue = MA2) at MOI 0.1 and culture supernatant titered by $CCID_{50}$ at day 0, 1, 2 and 3 post-infection. n = at least 3 per virus strain per cell line. Statistics was determined using t-test at the indicated timepoint. For 'A' and 'B', MA1 and MA2 data combined was compared with ancestral, alpha and beta data combined. For 'C' MA1 was compared with MA2.

Figure 5. MA1 and MA2 SARS-CoV-2 replicates to high titers in mouse lung bronchial epithelium and nasal turbinates. C57BL/6J mice were infected with MA1 or MA2 and lungs **(A)** or nasal turbinates **(B)** collected at day 2, 4 or 7 post-infection and titered by $CCID_{50}$ assay.

Statistics were determined using t-test. **C)** Heart, brain, small intestine, colon, liver, kidney, and spleen were titered at day 2 and 4. n = 4 per virus strain per timepoint. **D)** Percent weight change for mice in A-C (n=24 on day 2, n=16 on day 4 and n=8 on day 7). Data represents the mean percent weight loss from day 0 and error bars represent SEM. **E)** Anti-SARS-CoV-2 spike IHC (brown staining) in MA1 or MA2 infected C57BL/6J mouse lungs on day 2, 4 or 6, QLD02 infected K18-hACE2 lungs, QLD02 infected mACE2-hACE2 lungs, or naïve mice ('a' = alveolar spaces, 'b' = bronchioles). Images are representative of lung sections from 4 mice at each time point.

Figure 6. C57BL/6J mice infected with MA1 and MA2 have severe lung histopathology. A) Representative images of H&E stained lung sections for naïve or MA1 and MA2 SARS-CoV-2 infected C57BL/6J mice. Bronchiolar sloughing is indicated by arrows, smooth muscle hyperplasia by stars, bronchial bleeding/oedema by plus signs and collapse of alveolar spaces by rectangle boxes. 'a' = alveolar spaces, 'b' = bronchioles. Images are representative of lung sections from 4 mice at each time point. **B)** Ratio of nuclear (blue/dark purple) to non-nuclear (red) staining of H&E stained lung sections (a measure of leukocyte infiltration). Data is the average of 4 mice per group, with 3 sections scanned per lung and values averaged to produce one value for each lung. Error bars represent SEM. Statistics by t-tests for all MA1 timepoints combined vs naïve and all MA2 timepoints combined vs naïve. **C)** Image analysis to measure lung consolidation quantitated as areas of white space (unstained air spaces) per μm^2. Data is the average of 4 mice per group, with 3 sections scanned per lung and values averaged to produce one value for each lung. Error bars represent SEM. Statistics by t-tests for naïve vs day 7 MA1.

MATERIALS and METHODS

Ethics statement and regulatory compliance

All mouse work was conducted in accordance with the "Australian code for the care and use of animals for scientific purposes" as defined by the National Health and Medical Research Council of Australia. Mouse work was approved by the QIMR Berghofer Medical Research Institute animal ethics committee (P3600, A2003-607). For intrapulmonary inoculations, mice were anesthetized using isoflurane. Mice were euthanized using CO_2 or cervical dislocation.

Breeding and use of GM mice was approved under a Notifiable Low Risk Dealing (NLRD) Identifier: NLRD_Suhrbier_Oct2020: NLRD 1.1(a). Cloning and use of lentiviral vectors for transduction of ACE2 in to mice lungs and cell lines was approved under an NLRD (OGTR identifier: NLRD_Suhrbier_Feb2021: NLRD 2.1(l), NLRD 2.1(m)).

All infectious SARS-CoV-2 work was conducted in a dedicated suite in a biosafety level-3 (PC3) facility at the QIMR Berghofer MRI (Australian Department of Agriculture, Water and the Environment certification Q2326 and Office of the Gene Technology Regulator certification 3445).

Cell lines and SARS-CoV-2 culture

Vero E6 (C1008, ECACC, Wiltshire, England; obtained via Sigma Aldrich, St. Louis, MO, USA), Lenti-X 293T (Takara Bio), AE17 (a gift from Dr Delia Nelson, Faculty of Health Sciences, Curtin Medical School), NIH-3T3 (American Type Culture Collection, ATCC, CRL-1658), LLC-PK1 (a gift from Prof. Roy Hall, UQ), A549 (ATCC CCL-185) and HeLa (ATCC-CLL 2) cells were cultured in medium comprising DMEM for Lenti-X 293T and A549 cells, M199 for LLC-PK1 cells or RPMI1640 for all others (Gibco) supplemented with 10% fetal calf serum (FCS), penicillin (100□IU/ml)/streptomycin (100□µg/ml) (Gibco/Life Technologies) and L-glutamine (2 mM) (Life Technologies). Cells were cultured at 37°C and 5% CO_2. Cells were

routinely checked for mycoplasma (MycoAlert Mycoplasma Detection Kit MycoAlert, Lonza) and FCS was assayed for endotoxin contamination before purchase (55).

The SARS-CoV-2 isolates were kindly provided by Dr Alyssa Pyke (Queensland Health Forensic & Scientific Services, Queensland Department of Health, Brisbane, Australia). The viruses (hCoV-19/Australia/QLD02/2020, Alpha variant hCoV-19/Australia/QLD1517/2021 and Beta variant hCoV-19/Australia/QLD1520/2020) were isolated from patients and sequences deposited at GISAID (https://www.gisaid.org/; after registration and login, sequences can be downloaded from https://www.epicov.org/epi3/frontend#1707af). Virus stocks were generated by infection of Vero E6 cells at multiplicity of infection (MOI)≈0.01, with supernatant collected after 2-3 days, cell debris removed by centrifugation at 3000 x g for 15 min at 4°C, and virus aliquoted and stored at -80°C. Virus titers were determined using standard $CCID_{50}$ assays (see below). The virus was determined to be mycoplasma free using co-culture with a non-permissive cell line (i.e. HeLa) and Hoechst staining as described (56).

$CCID_{50}$ assays

Vero E6 cells were plated into 96 well flat bottom plates at $2x10^4$ cells per well in 100 µl of medium. For tissue titer, tissue was homogenized in tubes each containing 4 ceramic beads twice at 6000 x g for 15 seconds, followed by centrifugation twice at 21000 x g for 5 min before 5 fold serial dilutions in 100 µl RPMI1640 supplemented with 2% FCS. For cell culture supernatant, 10 fold serial dilutions were performed in 100 µl RPMI1640 supplemented with 2% FCS. 100 µl of serially diluted samples were added to Vero E6 cells and the plates cultured for 5 days at 37°C and 5% CO_2. The virus titer was determined by the method of Spearman and Karber (a convenient Excel $CCID_{50}$ calculator is available at https://www.klinikum.uni-

heidelberg.de/zentrum-fuer-infektiologie/molecular-virology/welcome/downloads).

SARS-CoV-2 passaging in hACE2 and mACE2 co-cultures

Lentivirus encoding hACE2, mACE2 or mACE2-N31K/H353K was produced in HEK293T cells by plasmid transfection and was used to transduce HEK293T cells, as described previously (2). HEK293T-hACE2 or HEK293T-mACE2-N31K/H353K was mixed with equal cell numbers of HEK293T-mACE2, and 500,000 cells (i.e. 250,000 HEK293T-hACE2 or mACE2-N31K/H353K + 250,000 HEK293T-mACE2) were seeded in 6 well plates overnight. Co-cultures were infected with SARS-CoV-2 at MOI 0.1. Every 3-4 days, supernatant was collected and centrifuged at 2000 x g at 4°C for 5 min, and 200 µl was added to fresh co-cultures and the remaining was stored at -80°C. This was performed a total of 9 times before 1 ml was passaged on to HEK293T-mACE2 cells. After one passage in HEK293T-mACE2 cells, supernatant was used to infect new HEK293T-mACE2 cells for 2 hrs, then inoculum was removed and cells were washed 3 times with PBS and media replaced. Supernatant was harvested at 0 hr and 72 hrs post infection for virus titration by $CCID_{50}$ to confirm virus replication in mACE2 expressing cells. Virus was then passaged one additional time in HEK293T-mACE2 cells and supernatant stored at -80°C for use in sequencing and mouse infections.

For growth kinetics experiments, HEK293T, HEK293T-hACE2 and HEK293T-mACE2, NIH-3T3, AE17, A549, HeLa or LLC-PK1 cells were infected with SARS-CoV-2 (QLD02, MA1, MA2, Alpha or Beta) at MOI 0.1 for 1 hr at 37°C, cells were washed with PBS and media replaced. Culture supernatant was harvested at the indicated time points and titered by CCID50 assay as described.

Mouse intrapulmonary SARS-CoV-2 infection

Female C57BL/6J mice (~ 6 months old at the time of infection) were purchased from Animal Resources Centre (Canning Vale, WA, Australia). The conditions the mice were kept are as follows: light = 12:12 h dark/light cycle, 7:45 a.m. sunrise and 7:45 p.m. sunset, 15 min light dark and dark light ramping time. Enclosures: M.I.C.E cage (Animal Care Systems, Colorado, USA). Ventilation: 100% fresh air, eight complete air exchange/h/rooms. In-house enrichment: paper cups (Impact-Australia); tissue paper, cardboard rolls. Bedding: PuraChips (Able scientific) (aspen fine). Food: Double bagged norco rat and mouse pellet (AIRR, Darra, QLD). Water: deionized water acidified with HCl (pH = 3.2). Mice were anesthetized using isoflurane and given an intrapulmonary inoculation of approximately 10^4 to 10^5 $CCID_{50}$ SARS-CoV-2 delivered via the intranasal route in 50 µl. Mice were sacrificed by cervical dislocation at day 2, 4 or 7 and lungs, nasal turbinates, brain, small intestine, colon, liver, kidney and spleen were collected. Right lung and all other organs were immediately homogenized in tubes each containing 4 beads twice at 6000 x g for 15 seconds, and used in tissue titration as described above. Left lungs were fixed in 10% formalin for histology.

K18-hACE2 mice (strain B6.Cg-Tg(K18-ACE2)2Prlmn/J, JAX Stock No: 034860) (57) were purchased from The Jackson Laboratory, USA, and bred and maintained in-house at QIMRB as heterozygotes by crossing with C57BL/6J mice. Mice were genotyped using Extract-N-Amp Tissue PCR Kit (Sigma Aldrich) according to manufacturers' instructions with the following primers; Forward 5'-CTTGGTGATATGTGGGGTAGA-3' and Reverse 5'-CGCTTCATCTCCCACCACTT-3' (recommended by NIOBIOHN, Osaka, Japan). Thermocycling conditions were as follows; 94°C 3 min, 35 cycles of 94°C 30 s, 55.8 °C 30 s, 72°C 1 min, and final extension of 72°C 10 min.

525 mACE2-hACE2 mice were created by Phenomics Australia/Monash Genome
526 Modification Platform, and bred and maintained in-house at QIMRB as heterozygotes by
527 crossing with C57BL/6J mice. mACE2-hACE2 mouse line creation and genotyping is described
528 in Bishop *et al.* (in preparation).
529
530 **MA SARS-CoV-2 RNA sequencing**
531 RNA was purified from cell culture supernatant using NucleoSpin RNA Virus kit (Machery-
532 Nagel) as per manufacturers' instructions. RNA from mouse lung homogenate was purified
533 using TRIzol (Life Technologies) as per manufacturers' instructions.
534 RNA concentration and quality was measured using TapeStation D1K TapeScreen assay
535 (Agilent). cDNA libraries were prepared using the Illumina TruSeq Stranded mRNA library
536 prep kit and the sequencing performed on the Illumina Nextseq 550 platform generating 75bp
537 paired end reads. Per base sequence quality for >90% bases was above Q30 for all samples. The
538 quality of raw sequencing reads was assessed using FastQC (58) (v0.11.80), and trimmed using
539 Cutadapt (59) (v2.3) to remove adapter sequences and low-quality bases. Trimmed reads were
540 aligned using STAR (60) (v2.7.1a) to a SARS-CoV-2 isolate Wuhan-Hu-1 (NC_045512.2;
541 29903 bp). Aligned reads were viewed using Integrative Genome Viewer (IGV) (61), and any
542 position with >20% change compared to the reference genome was manually curated. SAMtools
543 mpileup was used to produce a consensus sequence from mapped reads (62).
544
545 **Analysis of RNA-Seq data from cell lines**
546 Raw data (fastq files) from RNA-Seq of HEK293T, HeLa, 3T3, A549, A549 + influenza, Caco2
547 and Calu3 cells was obtained from the Sequence Read Archive (SRA). 2-3 samples from the

control experimental groups from at least two studies per cell line were analyzed as follows: Fastq files were trimmed of adapter sequences using Cutadapt, mapped to the human reference genome GRCh38 or the mouse reference genome GRCm39 using STAR aligner and TPM normalized gene counts were generated using RSEM. SRA run accessions; HEK293T = SRR16495652, SRR16495651, SRR16495650, SRR16218637, SRR16218638. HeLa = SRR15733492, SRR15733493, SRR15733494, SRR16904840, SRR16904840, SRR16904842. 3T3 = SRR14067064, SRR14067065, SRR9326749, SRR9326749, SRR9326751. A549 = SRR16201279, SRR16201280, SRR16201280, SRR15410446, SRR15410446. A549 + influenza = SRR13161304, SRR13161305. Caco2 = SRR13493599, SRR13493596, SRR10416443, SRR10416444, SRR10416444. Calu3 = SRR12709014, SRR12709014, SRR11234095, SRR11234094.

SARS-CoV-2 amino acid change analyses and modelling

GISAID (https://www.gisaid.org/phylodynamics/global/nextstrain/) (63) data was accessed through CoV-GLUE-Viz (http://cov-glue-viz.cvr.gla.ac.uk/mutations.php), and the count and proportion of each amino acid change in MA viruses were recorded on 7th December 2021, with the last CoV-GLUE-Viz update reported as 23rd November 2021.

PyMOL v4.60 (Schrodinger) was used for mutagenesis of the crystal structure of SARS-CoV-2 spike bound with ACE2 from the protein data bank (7DF4) (64).

Lung histopathology and immunohistochemistry

Lungs were fixed in 10% formalin, embedded in paraffin, and sections stained with H&E (Sigma Aldrich). Slides were scanned using Aperio AT Turbo (Aperio, Vista, CA USA) and analyzed

using Aperio ImageScope software (LeicaBiosystems, Mt Waverley, Australia) (v10) and the Positive Pixel Count v9 algorithm. Automatic quantitation of white space was undertaken using QuPath v0.2.3 (65). Immunohistochemistry for SARS-CoV-2 antigen was undertaken using mouse anti-SARS-CoV-2 spike monoclonal antibody 1E8 (Hobson-Peters *et al*. in preparation) as described previously (2).

Suspension cell infection and crystal violet statining

HEK293T or HEK293T-hACE2 cells were detached using trypsin (ThermoFisher scientific), TrypLE (ThermoFisher scientific), citric saline (135 mM KCl, 15 mM sodium citrate), or by mechanically detaching in culture media using a serological pipette. 10^4 cells per well were added to 96 well plates and infected with 100 $CCID_{50}$ MA1 either immediately or after overnight attachment of cells. After 4 days cells were fixed and stained by adding 50 µl formaldehyde (15% w/v) and crystal violet (0.1% w/v) (Sigma-Aldrich) overnight. The plates were washed in tap water, dried and images taken.

Statistics

Statistical analyses of experimental data were performed using IBM SPSS Statistics for Windows, Version 19.0 (IBM Corp., Armonk, NY, USA). The t-test was used when the difference in variances was <4, skewness was > -2 and kurtosis was <2. Otherwise, the non-parametric Kolmogorov–Smirnov test or Kruskal-Wallis test was used.

SUPPPLEMENTARY FIGURE LEGENDS

Supplementary Figure 1. Orf1ab amino acid changes and prevalence in human isolates.

Supplementary Figure 2. RBD amino acid changes in MA1 and the Omicron variant. The structure of the spike RBD bound to hACE2 (PDB: 7df4) viewed in PyMOL. Red amino acids = QLD02 residues, and purple amino acids = changes from QLD02 in MA1 or Omicron variant.

Supplementary Figure 3. R408G amino acid change in MA2. The structure of the spike RBD bound to hACE2 (PDB: 7df4) viewed in PyMOL with R408 for QLD02 or G408 for MA2 colored in red. Green = hACE2. Blue = spike RBD.

Supplementary Figure 4. ACE2 counts per million for cell lines used in this study. Average ACE2 transcripts per million (TPM) is shown for Caco 2 (n=5), Calu3 (n=4), HEK293T (n=5), 3T3 (n=5), HeLa (n=6), A549 (n=5), A549 + influenza (n=2). Error bars represent SEM. Publically available data was downloaded from Sequence Read Archive (SRA) as per materials and methods.

Supplementary Figure 5. MA1 infection of HEK293T cells is less efficient when cells are in suspension. HEK293T or HEK293T-hACE2 cells were detached using trpsin, trpyLE, citric saline or mechanical detachment. Cells were aliquoted to 10^4 cells per well in 96 well plates and 100 CCID50 SARS-CoV-2 MA1 was immediately added per well. For overnight seeding, cells were infected the following day. Cells were incubated for 4 days and stained with crystal violet. Cytopathic effect (CPE) was counted when most of the cells in a well had died.

Supplementary Figure 6. RGD motif in the spike RBD. The 'RGD' motif in the spike RBD, which may interact with integrins, is highlighted in orange. E484 and Q498 for QLD02, D484 and H498 for MA1, and A484 and R498 for Omicron is highlighted in red.

Supplementary Figure 7. Integrin mRNA expression in cell lines. Mean ± SEM transcripts per million (TPM) for integrin mRNA's in HEK293T (n=5, black), 3T3 (n=5, red), HeLa (n=6, blue) and A549 (n=5, green) cell lines. Publically available data was downloaded from Sequence Read Archive (SRA) as per materials and methods.

REFERENCES

1. Wu F, Zhao S, Yu B, Chen Y-M, Wang W, Song Z-G, et al. A new coronavirus associated with human respiratory disease in China. Nature. 2020;579(7798):265-9.
2. Rawle DJ, Le TT, Dumenil T, Yan K, Tang B, Nguyen W, et al. ACE2-lentiviral transduction enables mouse SARS-CoV-2 infection and mapping of receptor interactions. PLOS Pathogens. 2021;17(7):e1009723.
3. Starr TN, Zepeda SK, Walls AC, Greaney AJ, Veesler D, Bloom JD. ACE2 binding is an ancestral and evolvable trait of sarbecoviruses. bioRxiv. 2021:2021.07.17.452804.
4. Hu B, Zeng L-P, Yang X-L, Ge X-Y, Zhang W, Li B, et al. Discovery of a rich gene pool of bat SARS-related coronaviruses provides new insights into the origin of SARS coronavirus. PLOS Pathogens. 2017;13(11):e1006698.
5. Cele S, Jackson L, Khan K, Khoury DS, Moyo-Gwete T, Tegally H, et al. SARS-CoV-2 Omicron has extensive but incomplete escape of Pfizer BNT162b2 elicited neutralization and requires ACE2 for infection. medRxiv. 2021:2021.12.08.21267417.
6. Shuai H, Chan JF-W, Yuen TT-T, Yoon C, Hu J-C, Wen L, et al. Emerging SARS-CoV-2 variants expand species tropism to murines. EBioMedicine. 2021;73.
7. Puray-Chavez M, LaPak KM, Schrank TP, Elliott JL, Bhatt DP, Agajanian MJ, et al. Systematic analysis of SARS-CoV-2 infection of an ACE2-negative human airway cell. Cell Reports. 2021:109364.
8. Muñoz-Fontela C, Dowling WE, Funnell SGP, Gsell P-S, Riveros-Balta AX, Albrecht RA, et al. Animal models for COVID-19. Nature. 2020;586(7830):509-15.
9. Shou S, Liu M, Yang Y, Kang N, Song Y, Tan D, et al. Animal Models for COVID-19: Hamsters, Mouse, Ferret, Mink, Tree Shrew, and Non-human Primates. Frontiers in Microbiology. 2021;12(2357).
10. Amarilla AA, Sng JDJ, Parry R, Deerain JM, Potter JR, Setoh YX, et al. A versatile reverse genetics platform for SARS-CoV-2 and other positive-strand RNA viruses. Nature Communications. 2021:Forthcoming.
11. Leist SR, Dinnon KH, Schäfer A, Tse LV, Okuda K, Hou YJ, et al. A Mouse-Adapted SARS-CoV-2 Induces Acute Lung Injury and Mortality in Standard Laboratory Mice. Cell. 2020;183(4):1070-85.e12.
12. Zhang Y, Huang K, Wang T, Deng F, Gong W, Hui X, et al. SARS-CoV-2 Rapidly Adapts in Aged BALB/c Mice and Induces Typical Pneumonia. Journal of Virology. 2021;95(11):e02477-20.
13. Huang K, Zhang Y, Hui X, Zhao Y, Gong W, Wang T, et al. Q493K and Q498H substitutions in Spike promote adaptation of SARS-CoV-2 in mice. EBioMedicine. 2021;67:103381.
14. Gu H, Chen Q, Yang G, He L, Fan H, Deng Y-Q, et al. Adaptation of SARS-CoV-2 in BALB/c mice for testing vaccine efficacy. Science. 2020;369(6511):1603.
15. Wang J, Shuai L, Wang C, Liu R, He X, Zhang X, et al. Mouse-adapted SARS-CoV-2 replicates efficiently in the upper and lower respiratory tract of BALB/c and C57BL/6J mice. Protein Cell. 2020;11(10):776-82.
16. Dinnon KH, Leist SR, Schäfer A, Edwards CE, Martinez DR, Montgomery SA, et al. A mouse-adapted model of SARS-CoV-2 to test COVID-19 countermeasures. Nature. 2020;586(7830):560-6.
17. Palermo PM, Orbegozo J, Watts DM, Morrill JC. SARS-CoV-2 Neutralizing Antibodies in White-Tailed Deer from Texas. Vector Borne Zoonotic Dis. 2021.
18. Díaz AV, Walker M, Webster JP. Surveillance and control of SARS-CoV-2 in mustelids: An evolutionary perspective. Evol Appl. 2021.
19. Langereis MA, Albulescu IC, Stammen-Vogelzangs J, Lambregts M, Stachura K, Miller S, et al. An alphavirus replicon-based vaccine expressing a stabilized Spike antigen induces protective immunity and prevents transmission of SARS-CoV-2 between cats. npj Vaccines. 2021;6(1):122.
20. Welkers MRA, Han AX, Reusken CBEM, Eggink D. Possible host-adaptation of SARS-CoV-2 due to improved ACE2 receptor binding in mink. Virus Evolution. 2021;7(1).

667 21. Chandler JC, Bevins SN, Ellis JW, Linder TJ, Tell RM, Jenkins-Moore M, et al. SARS-CoV-2
668 exposure in wild white-tailed deer (Odocoileus virginianus). Proceedings of the
669 National Academy of Sciences. 2021;118(47):e2114828118.
670 22. Liu Z, Zheng H, Lin H, Li M, Yuan R, Peng J, et al. Identification of Common Deletions in the Spike
671 Protein of Severe Acute Respiratory Syndrome Coronavirus 2. Journal of Virology. 2020;94(17):e00790-
672 20.
673 23. Watanabe Y, Allen JD, Wrapp D, McLellan JS, Crispin M. Site-specific glycan analysis of the SARS-
674 CoV-2 spike. Science (New York, NY). 2020;369(6501):330-3.
675 24. Meng B, Kemp SA, Papa G, Datir R, Ferreira IATM, Marelli S, et al. Recurrent emergence of SARS-
676 CoV-2 spike deletion H69/V70 and its role in the Alpha variant B.1.1.7. Cell Reports. 2021;35(13):109292.
677 25. Dieterle ME, Haslwanter D, Bortz RH, 3rd, Wirchnianski AS, Lasso G, Vergnolle O, et al. A
678 Replication-Competent Vesicular Stomatitis Virus for Studies of SARS-CoV-2 Spike-Mediated Cell Entry
679 and Its Inhibition. Cell Host Microbe. 2020;28(3):486-96.e6.
680 26. Rathnasinghe R, Jangra S, Cupic A, Martínez-Romero C, Mulder LCF, Kehrer T, et al. The N501Y
681 mutation in SARS-CoV-2 spike leads to morbidity in obese and aged mice and is neutralized by
682 convalescent and post-vaccination human sera. medRxiv. 2021:2021.01.19.21249592.
683 27. Greaney AJ, Starr TN, Barnes CO, Weisblum Y, Schmidt F, Caskey M, et al. Mapping mutations to
684 the SARS-CoV-2 RBD that escape binding by different classes of antibodies. Nature Communications.
685 2021;12(1):4196.
686 28. Richard M, Kok A, de Meulder D, Bestebroer TM, Lamers MM, Okba NMA, et al. SARS-CoV-2 is
687 transmitted via contact and via the air between ferrets. Nature Communications. 2020;11(1):3496.
688 29. Hoffmann M, Kleine-Weber H, Schroeder S, Krüger N, Herrler T, Erichsen S, et al. SARS-CoV-2
689 Cell Entry Depends on ACE2 and TMPRSS2 and Is Blocked by a Clinically Proven Protease Inhibitor. Cell.
690 2020;181(2):271-80.e8.
691 30. Chu H, Chan JF-W, Yuen TT-T, Shuai H, Yuan S, Wang Y, et al. Comparative tropism, replication
692 kinetics, and cell damage profiling of SARS-CoV-2 and SARS-CoV with implications for clinical
693 manifestations, transmissibility, and laboratory studies of COVID-19: an observational study. The Lancet
694 Microbe. 2020;1(1):e14-e23.
695 31. Liu Y, Hu G, Wang Y, Ren W, Zhao X, Ji F, et al. Functional and genetic analysis of viral receptor
696 ACE2 orthologs reveals a broad potential host range of SARS-CoV-2. Proceedings of the National
697 Academy of Sciences. 2021;118(12):e2025373118.
698 32. Ichimura T, Mori Y, Aschauer P, Padmanabha Das KM, Padera RF, Weins A, et al. KIM-1/TIM-1 is
699 a Receptor for SARS-CoV-2 in Lung and Kidney. medRxiv. 2020.
700 33. DiPiazza AT, Leist SR, Abiona OM, Moliva JI, Werner A, Minai M, et al. COVID-19 vaccine mRNA-
701 1273 elicits a protective immune profile in mice that is not associated with vaccine-enhanced disease
702 upon SARS-CoV-2 challenge. Immunity. 2021;54(8):1869-82.e6.
703 34. Winkler Emma S, Chen Rita E, Alam F, Yildiz S, Case James B, Uccellini Melissa B, et al. SARS-CoV-
704 2 causes lung infection without severe disease in human ACE2 knock-in mice. Journal of Virology.
705 2021;0(ja):JVI.01511-21.
706 35. Prow NA, Hirata TDC, Tang B, Larcher T, Mukhopadhyay P, Alves TL, et al. Exacerbation of
707 Chikungunya Virus Rheumatic Immunopathology by a High Fiber Diet and Butyrate. Front Immunol.
708 2019;10:2736-.
709 36. Wang S, Qiu Z, Hou Y, Deng X, Xu W, Zheng T, et al. AXL is a candidate receptor for SARS-CoV-2
710 that promotes infection of pulmonary and bronchial epithelial cells. Cell Res. 2021;31(2):126-40.
711 37. Puray-Chavez M, LaPak KM, Schrank TP, Elliott JL, Bhatt DP, Agajanian MJ, et al. Systematic
712 analysis of SARS-CoV-2 infection of an ACE2-negative human airway cell. Cell Reports.
713 2021;36(2):109364.

714 38. Amraei R, Yin W, Napoleon MA, Suder EL, Berrigan J, Zhao Q, et al. CD209L/L-SIGN and
715 CD209/DC-SIGN Act as Receptors for SARS-CoV-2. ACS Cent Sci. 2021;7(7):1156-65.
716 39. Wang K, Chen W, Zhang Z, Deng Y, Lian J-Q, Du P, et al. CD147-spike protein is a novel route for
717 SARS-CoV-2 infection to host cells. Signal Transduction and Targeted Therapy. 2020;5(1):283.
718 40. Simons P, Rinaldi DA, Bondu V, Kell AM, Bradfute S, Lidke DS, et al. Integrin activation is an
719 essential component of SARS-CoV-2 infection. Sci Rep. 2021;11(1):20398.
720 41. Nader D, Fletcher N, Curley GF, Kerrigan SW. SARS-CoV-2 uses major endothelial integrin αvβ3
721 to cause vascular dysregulation in-vitro during COVID-19. PLoS One. 2021;16(6):e0253347.
722 42. Park EJ, Myint PK, Appiah MG, Darkwah S, Caidengbate S, Ito A, et al. The Spike Glycoprotein of
723 SARS-CoV-2 Binds to β1 Integrins Expressed on the Surface of Lung Epithelial Cells. Viruses. 2021;13(4).
724 43. Makowski L, Olson-Sidford W, J WW. Biological and Clinical Consequences of Integrin Binding via
725 a Rogue RGD Motif in the SARS CoV-2 Spike Protein. Viruses. 2021;13(2).
726 44. Dakal TC. SARS-CoV-2 attachment to host cells is possibly mediated via RGD-integrin interaction
727 in a calcium-dependent manner and suggests pulmonary EDTA chelation therapy as a novel treatment
728 for COVID 19. Immunobiology. 2021;226(1):152021.
729 45. Sigrist CJ, Bridge A, Le Mercier P. A potential role for integrins in host cell entry by SARS-CoV-2.
730 Antiviral Res. 2020;177:104759.
731 46. Starr TN, Greaney AJ, Hilton SK, Ellis D, Crawford KHD, Dingens AS, et al. Deep Mutational
732 Scanning of SARS-CoV-2 Receptor Binding Domain Reveals Constraints on Folding and ACE2 Binding. Cell.
733 2020;182(5):1295-310.e20.
734 47. Liu Z, Zheng H, Lin H, Li M, Yuan R, Peng J, et al. Identification of Common Deletions in the Spike
735 Protein of Severe Acute Respiratory Syndrome Coronavirus 2. Journal of Virology.94(17):e00790-20.
736 48. Laporte M, Raeymaekers V, Van Berwaer R, Vandeput J, Marchand-Casas I, Thibaut H-J, et al.
737 The SARS-CoV-2 and other human coronavirus spike proteins are fine-tuned towards temperature and
738 proteases of the human airways. PLOS Pathogens. 2021;17(4):e1009500.
739 49. Johnson BA, Xie X, Bailey AL, Kalveram B, Lokugamage KG, Muruato A, et al. Loss of furin
740 cleavage site attenuates SARS-CoV-2 pathogenesis. Nature. 2021;591(7849):293-9.
741 50. Peacock TP, Goldhill DH, Zhou J, Baillon L, Frise R, Swann OC, et al. The furin cleavage site in the
742 SARS-CoV-2 spike protein is required for transmission in ferrets. Nature Microbiology. 2021;6(7):899-
743 909.
744 51. Zhao MM, Yang WL, Yang FY, Zhang L, Huang WJ, Hou W, et al. Cathepsin L plays a key role in
745 SARS-CoV-2 infection in humans and humanized mice and is a promising target for new drug
746 development. Signal Transduct Target Ther. 2021;6(1):134.
747 52. Liu T, Luo S, Libby P, Shi G-P. Cathepsin L-selective inhibitors: A potentially promising treatment
748 for COVID-19 patients. Pharmacol Ther. 2020;213:107587-.
749 53. Li K, Shen Y, Miller MA, Stabenow J, Williams RW, Lu L. Differing susceptibility of C57BL/6J and
750 DBA/2J mice—parents of the murine BXD family, to severe acute respiratory syndrome coronavirus
751 infection. Cell & Bioscience. 2021;11(1):137.
752 54. Winkler ES, Bailey AL, Kafai NM, Nair S, McCune BT, Yu J, et al. SARS-CoV-2 infection of human
753 ACE2-transgenic mice causes severe lung inflammation and impaired function. Nature Immunology.
754 2020;21(11):1327-35.
755 55. Johnson BJ, Le TT, Dobbin CA, Banovic T, Howard CB, Flores Fde M, et al. Heat shock protein 10
756 inhibits lipopolysaccharide-induced inflammatory mediator production. J Biol Chem. 2005;280(6):4037-
757 47.
758 56. La Linn M, Bellett AJ, Parsons PG, Suhrbier A. Complete removal of mycoplasma from viral
759 preparations using solvent extraction. J Virol Methods. 1995;52(1-2):51-4.

57. McCray PB, Jr., Pewe L, Wohlford-Lenane C, Hickey M, Manzel L, Shi L, et al. Lethal infection of K18-hACE2 mice infected with severe acute respiratory syndrome coronavirus. J Virol. 2007;81(2):813-21.
58. Simons A. A quality control tool for high throughput sequence data. Available online: https://www.bioinformatics.babraham.ac.uk/projects/fastqc. 2010.
59. Martin M. Cutadapt removes adapter sequences from high-throughput sequencing reads. 2011. 2011;17(1):3.
60. Dobin A, Davis CA, Schlesinger F, Drenkow J, Zaleski C, Jha S, et al. STAR: ultrafast universal RNA-seq aligner. Bioinformatics. 2013;29(1):15-21.
61. Robinson JT, Thorvaldsdóttir H, Winckler W, Guttman M, Lander ES, Getz G, et al. Integrative genomics viewer. Nat Biotechnol. 2011;29(1):24-6.
62. Li H, Handsaker B, Wysoker A, Fennell T, Ruan J, Homer N, et al. The Sequence Alignment/Map format and SAMtools. Bioinformatics. 2009;25(16):2078-9.
63. Elbe S, Buckland-Merrett G. Data, disease and diplomacy: GISAID's innovative contribution to global health. Glob Chall. 2017;1(1):33-46.
64. Xu C, Wang Y, Liu C, Zhang C, Han W, Hong X, et al. Conformational dynamics of SARS-CoV-2 trimeric spike glycoprotein in complex with receptor ACE2 revealed by cryo-EM. Sci Adv. 2021;7(1).
65. Bankhead P, Loughrey MB, Fernández JA, Dombrowski Y, McArt DG, Dunne PD, et al. QuPath: Open source software for digital pathology image analysis. Scientific Reports. 2017;7(1):16878.

Figure 1

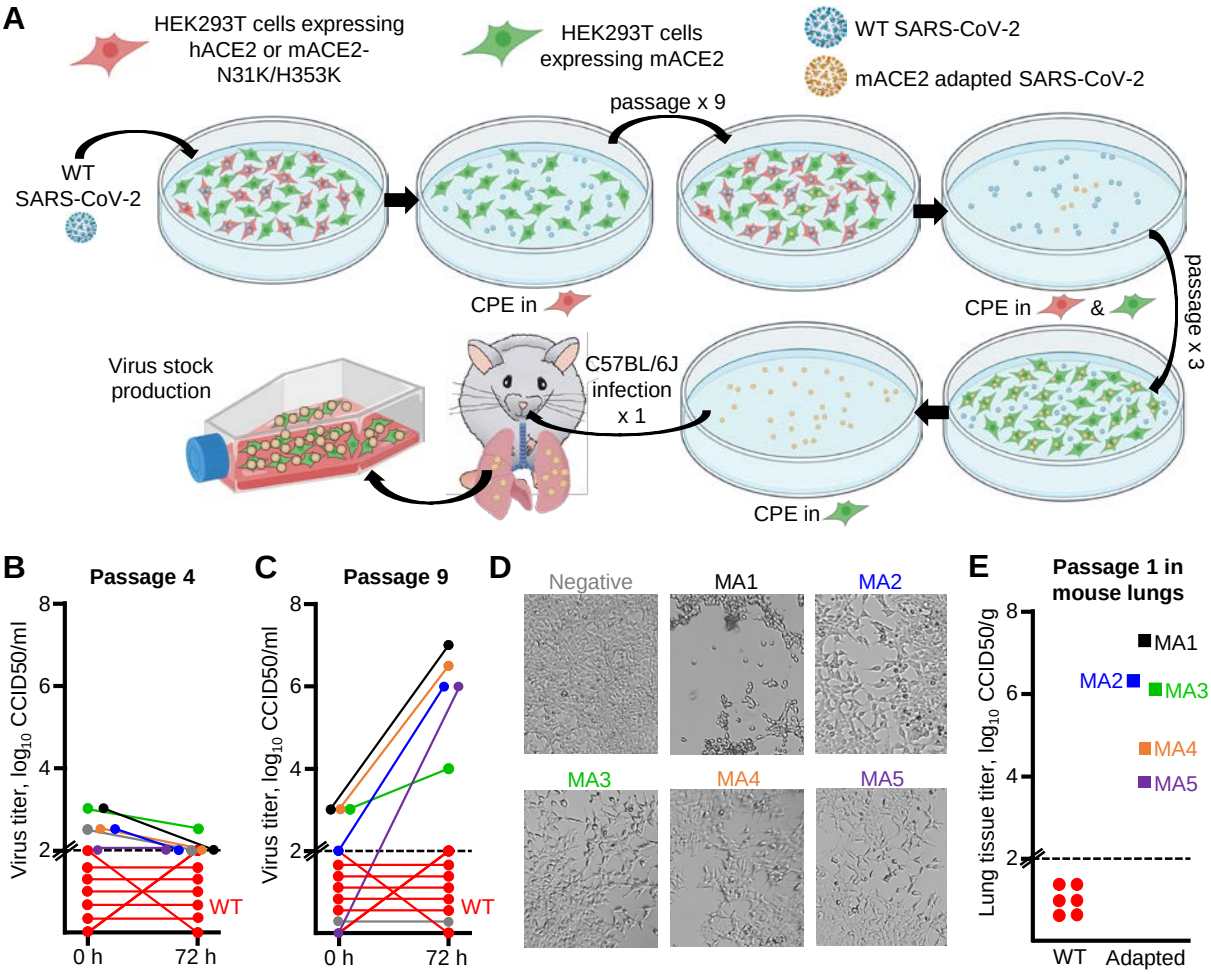

Figure 2

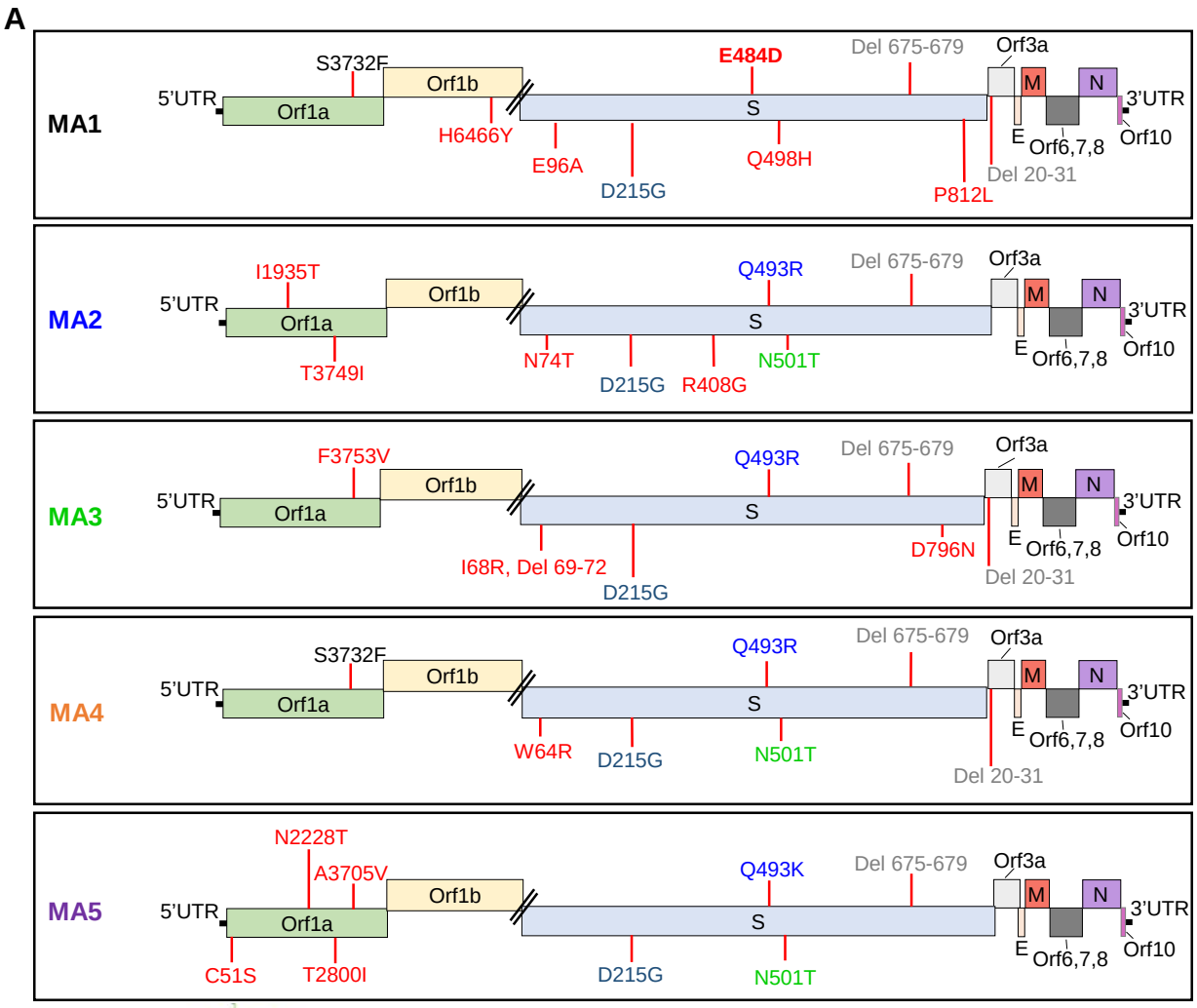

C

MA Spike changes	# isolates	Proportion (%)	Alpha	Beta	Gamma	Delta	Omicron
W64R	1238	0.0237					
I68R	41	0.0008					
69-70Δ	1157339	22.14	69-70Δ				69-70Δ
N74T	74	0.0014					
E96A	136	0.0026					
D215G	40238	7.696		D215G			
R408G	297	0.0057					
E484D	220	0.0042		E484K	E484K		E484A
Q493R	276	0.0053					Q493R
Q493K	176	0.0034					Q493R
Q498H	39	0.0008					Q498R
N501T	4780	0.0914	N501Y	N501Y	N501Y		N501Y
Del 675-679	179	0.0034					
D796N	256	0.0049					D796Y
P812L	5494	0.1051					

Figure 3

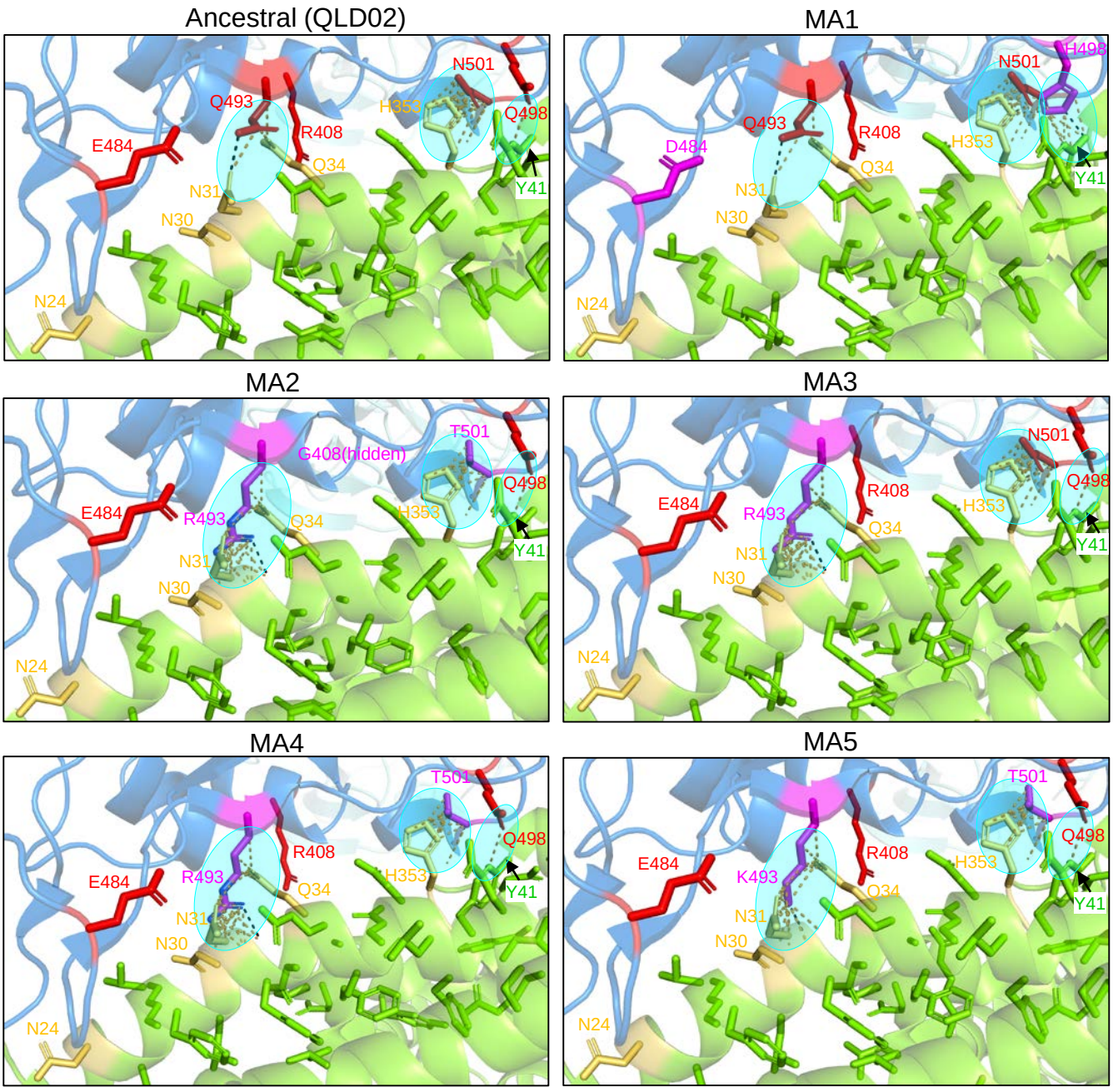

Spike RBD. **Spike RBD residues changed in any MA strain.** **Mutated spike RBD residue.** **ACE2.** **Mutated mACE2 residues.**

Interactions

Key changes:

- **RBD Q493K/R increases interactions with mACE2 N31 and Q34**
- **RBD Q498H increases interactions with mACE2 Y41 and H353**

Figure 4

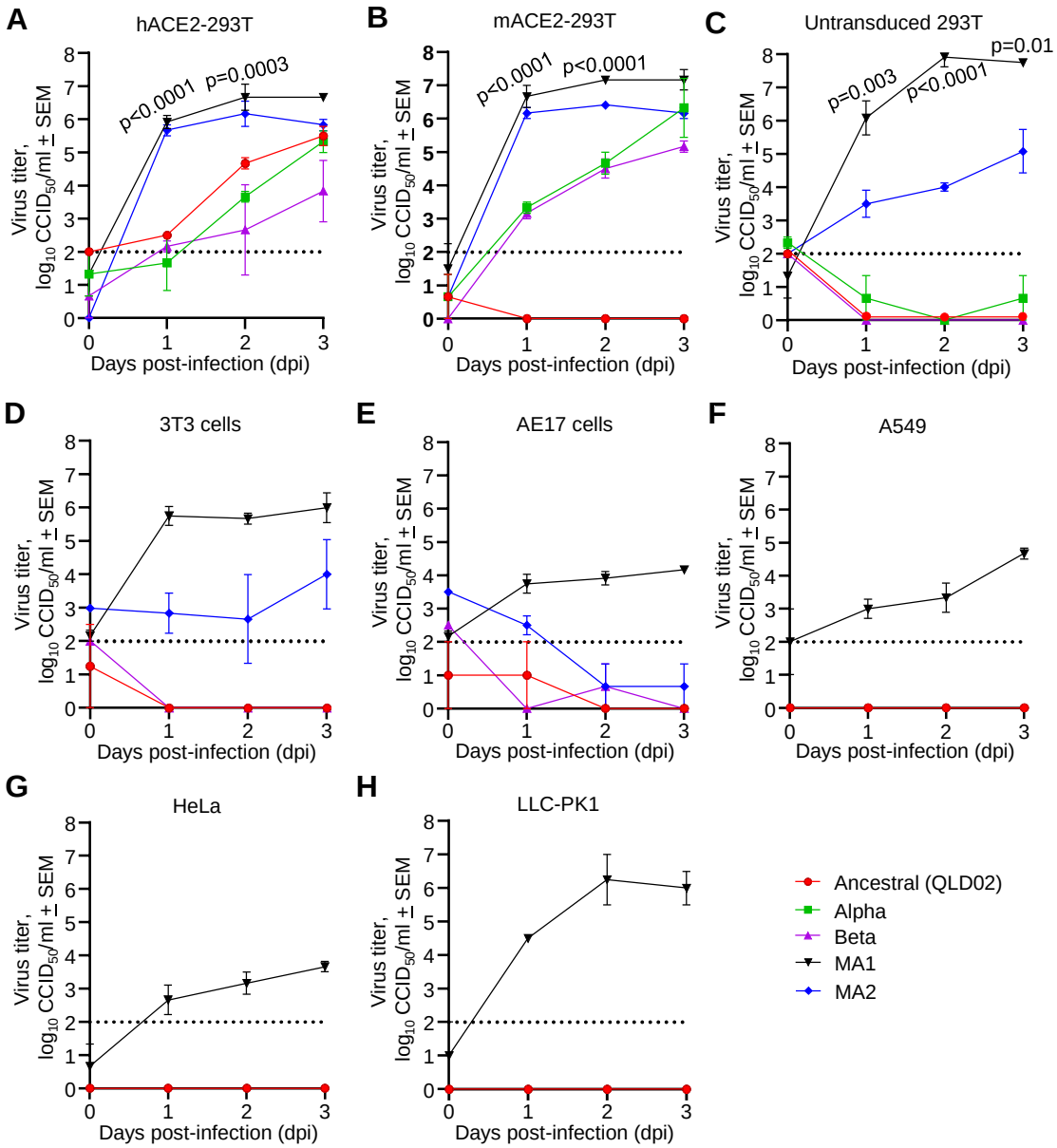

Figure 5

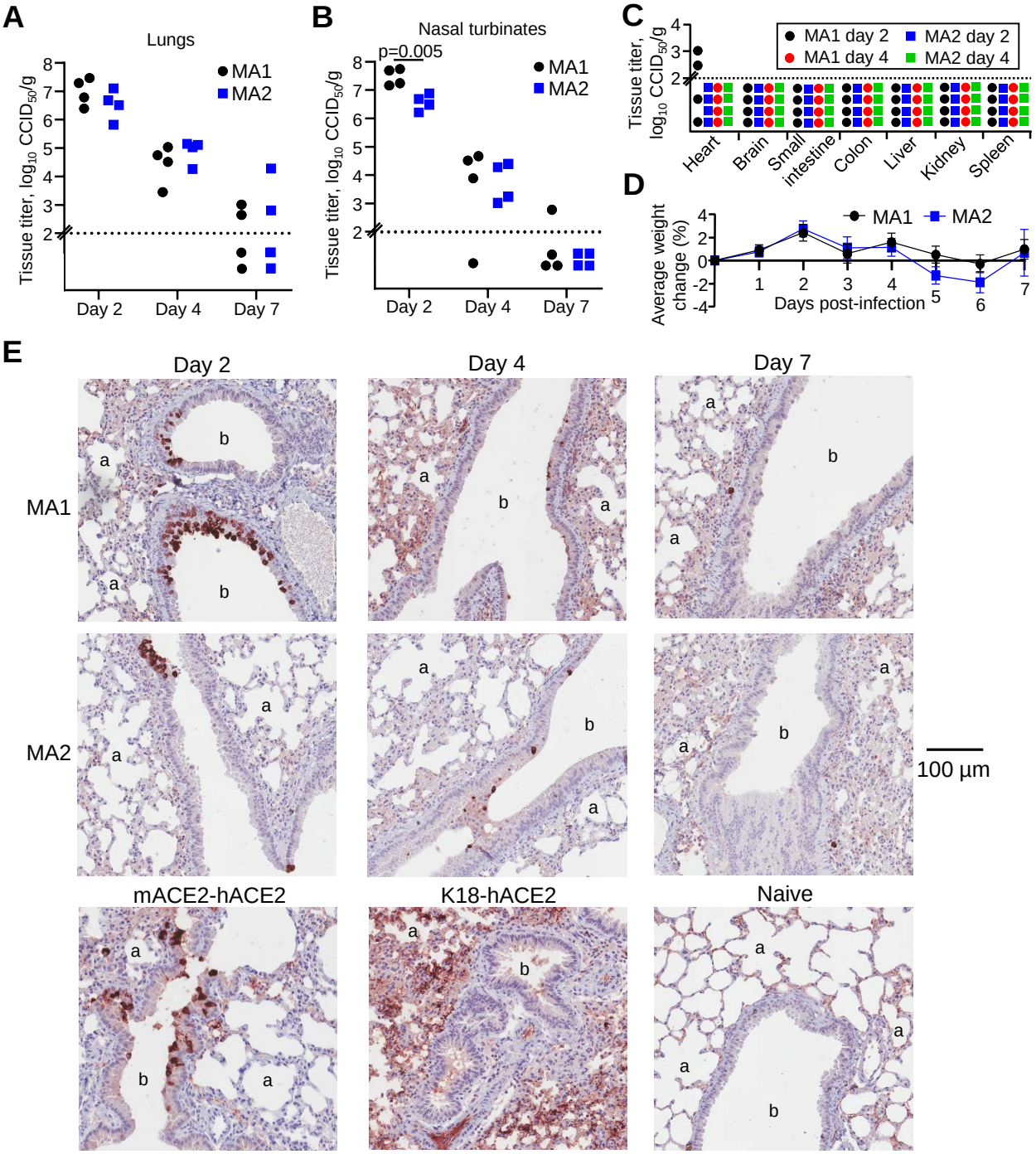

Figure 6